

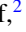
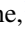


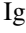
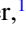

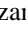
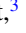
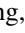




Realizing efficient topological temporal pumping in electrical circuits

Alexander Stegmaier ^{1,*} Hauke Brand ² Stefan Imhof ² Alexander Fritzsche ^{1,3} Tobias Helbig ¹ Tobias Hofmann ¹
Igor Boettcher ^{4,5} Martin Greiter ¹ Ching Hua Lee ⁶ Gaurav Bahl ⁷ Alexander Szameit ³ Tobias Kießling ²
Ronny Thomale ¹ and Lavi K. Upreti ^{1,8,†}

¹*Institute for Theoretical Physics and Astrophysics, University of Würzburg, Am Hubland, D-97074 Würzburg, Germany*

²*Physikalisches Institut and Röntgen Research Center for Complex Material Systems, Universität Würzburg, D-97074 Würzburg, Germany*

³*Institut für Physik, Universität Rostock, Albert-Einstein-Straße 23, 18059 Rostock, Germany*

⁴*Department of Physics, University of Alberta, Edmonton, Alberta, Canada T6G 2E1*

⁵*Theoretical Physics Institute, University of Alberta, Edmonton, Alberta, Canada T6G 2E1*

⁶*Department of Physics, National University of Singapore, Singapore 117542*

⁷*Department of Mechanical Science and Engineering, University of Illinois at Urbana-Champaign, Urbana, Illinois 61801, USA*

⁸*Fachbereich Physik, Universität Konstanz, D-78457 Konstanz, Germany*



(Received 28 June 2023; revised 13 November 2023; accepted 16 February 2024; published 2 April 2024)

Quantized adiabatic transport can occur when a system is slowly modulated over time. In most realizations, however, the efficiency of such transport is reduced by unwanted dissipation, back-scattering, and nonadiabatic effects. In this paper, we realize a topological adiabatic pump in an electrical circuit network that supports remarkably stable and long-lasting pumping of a voltage signal. We further characterize the topology of our system by deducing the Chern number from the measured edge band structure. To achieve this, the experimental setup makes use of active circuit elements that act as time-variable voltage-controlled inductors.

DOI: [10.1103/PhysRevResearch.6.023010](https://doi.org/10.1103/PhysRevResearch.6.023010)

I. INTRODUCTION

A Thouless pump [1] is an adiabatic charge pump, the transport properties of which are characterized by its underlying topology. The pumping process is achieved through the slow, periodic modulation of a potential, thereby inducing the transport of particles confined to a lattice despite the filled band and in absence of a net external field. The rate of transport is quantified by a Chern number associated with the energy bands of the system, which is a topological invariant of the same type as in the integer quantum Hall effect and Chern insulators [2]. However, for the Thouless pump, the Chern number is defined over a 1+1D periodic Brillouin zone constituted by one spatial dimension and time, in contrast to two spatial dimensions for the aforementioned effects. The topological protection ensures that the quantization of charge pumping is robust and unaffected by weak disorder [3].

Recently, interest in the topological Thouless pump resurged following the first experimental realizations in ultracold atomic systems [4–6]. Since then, implementations in a range of setups have emerged, including photonic waveguides

[7–10], acoustic metamaterials [11,12], and mechanical [13,14] systems as well as superconducting chips [15] or Josephson junctions [16,17]. Similar platforms are a seed for subsequent refinement and generalizations of the principal Thouless pump motif, as they allow for devising experiments that explore variations such as disordered pumping [8,13,18], pumping in continuous [19] or many-body systems [20], nonlinear pumping [21–23], non-Abelian pumps [10,12,24], and nonadiabatic [25] or Floquet pumping [26–29]. Realizations however typically exhibit considerable deviations from ideal topological pumping due to experimental constraints such as dissipation or nonadiabaticity, so that attainable pumping distances are limited to tens of lattice sites [4,9,12,19], though recent progress has been made in addressing this issue [30]. Electrical circuit lattices present a different suitable platform to overcome constraints of other metamaterial platforms, as they can emulate topological phenomena with high fidelity and promise to achieve topological pumping over long distances. They have recently gained relevance as a versatile platform for various topological systems [31–40]. The availability of quality components provides a versatile toolbox for the implementation of a wide range of models and effects. Other assets of electrical circuits are active circuit components such as operational amplifiers (op-amps) or analog multipliers. Op-amps in particular enabled the realization of chiral edge propagation [41], the non-Hermitian skin effect [42,43], active topological materials [44], and other topological phenomena [45–50]. Active elements also provide a gateway towards the implementation of temporally modulated systems in electrical circuits [51,52] and promise future realization of various Floquet phenomena.

*alexander.stegmaier@uni-wuerzburg.de

†lavi.upreti@uni-konstanz.de

Published by the American Physical Society under the terms of the [Creative Commons Attribution 4.0 International](https://creativecommons.org/licenses/by/4.0/) license. Further distribution of this work must maintain attribution to the author(s) and the published article's title, journal citation, and DOI.

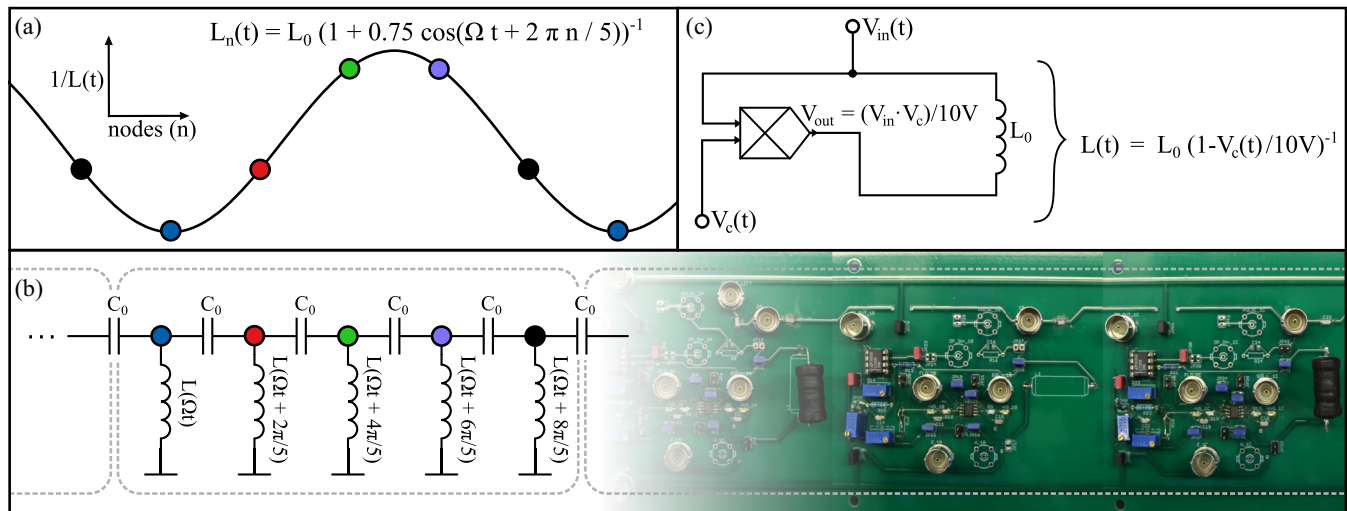


FIG. 1. Implementation of the Thouless pump in a circuit. (a) Variation of the inductance over space (nodes) and time. The inductors act as a cosine-shaped potential shifted over time to induce adiabatic pumping. (b) The circuit consists of a chain of capacitors, with each node connected to ground by a variable inductor. The dashed box indicates the unit cell of a periodic chain. On the left, a simplified circuit diagram of one unit cell is depicted, which blends into a photograph of a circuit board on the right, showing three circuit nodes. A detailed description of the circuit board can be found in the Appendix B. The complete circuit is made up of eight unit cells (40 nodes). (c) Schematic of the time-variable inductor. An analog multiplier creates a signal applied to an inductor connected to the node. The current flowing in and out of the subcircuit thus mimics that of a time-variable inductor to ground.

In this paper, we present the experimental realization of a topological Thouless pump in an electrical circuit. We employ time modulated circuit elements to implement the Aubry-André-Harper (AAH) model [53,54], which describes a particle on a one-dimensional (1D) chain, exposed to a periodic, time-dependent potential. For this, we devise circuit elements that function as a voltage controlled variable inductor, based on analog multipliers. In our classical platform, for small driving frequencies we are able to populate the lowest band uniformly in momentum space, allowing us to emulate topological bulk transport, which is typically a quantum-mechanical feature. Hence, the setup displays temporal pumping of a localized voltage signal that not only agrees extraordinarily well with theoretical predictions but also remains stable for a long time and over many ($>10^2$) lattice sites. Through impedance measurements, we resolve the band structure of the circuit and determine the topological Chern numbers of the bands from the edge state spectrum and the transport velocity of an adiabatically pumped signal.

II. IMPLEMENTING THE THOULESS PUMP

The driven AAH model is a 1D tight-binding model with a space- and time-modulated onsite potential, described by the Schrödinger equation

$$i \frac{d}{dt} \psi_n = j(\psi_{n+1} + \psi_{n-1}) + \lambda \cos(n\varphi + \tau) \psi_n, \quad (1)$$

where ψ_n is the wave function at site n , j is the hopping amplitude, λ is the amplitude of the onsite potential, φ is the phase difference between neighboring nodes due to spatial modulation, and τ is the pumping parameter to be modulated over time. The unit cell of the lattice is determined by the wavelength of the potential $2\pi/\varphi$. Note that if φ is 2π

times an irrational number, then the on-site term is quasiperiodic, and leads to a quasicrystal [55,56]. For our case, we choose a rational value of $\varphi = \frac{2\pi}{5}$, corresponding to a unit cell containing five nodes. The potential is illustrated in Fig. 1(a). Our circuit setup is a chain of eight unit cells (40 nodes).

The hopping terms between nodes are represented in the circuit by capacitors C_0 and the on-site terms are represented by variable inductors $L_n(\tau)$ [see Fig. 1(b)]. We employ a realization of variable inductors through analog multipliers [see Fig. 1(c)]. The effective inductance can be controlled through an external control voltage V_c . The resulting differential equation describing the nodal voltages V_m for input currents I_n at nodes $\{n\}$ is

$$\begin{aligned} \frac{d}{dt} I_n(t) &= \frac{d^2}{dt^2} C_0 (2\delta_{n,m} - \delta_{n+1,m} - \delta_{n-1,m}) V_m(t) \\ &\quad + (L_0)^{-1} [1 + \lambda \cos(n\varphi + \tau)] \delta_{n,m} V_m(t) \\ &= \frac{d^2}{dt^2} \Gamma_{nm} V_m(t) + \Lambda_{nm}(\tau) V_m(t). \end{aligned} \quad (2)$$

III. BAND STRUCTURES

We first investigate the properties of the circuit for fixed values of τ in order to reveal the band topology of the system over the parameter space of τ and lattice momentum k . The resonance band structure, i.e., the eigenfrequencies of the circuit, can be measured through the Green function $G(\omega)$ in the frequency domain ω . For this, we Fourier transform and invert Eq. (2), obtaining

$$V_n(\omega) = G_{nm}(\omega) I_m(\omega), \quad (3)$$

$$\text{with } G(\omega) = \left(i\omega\Gamma + \frac{1}{i\omega}\Lambda(\tau) \right)^{-1}. \quad (4)$$

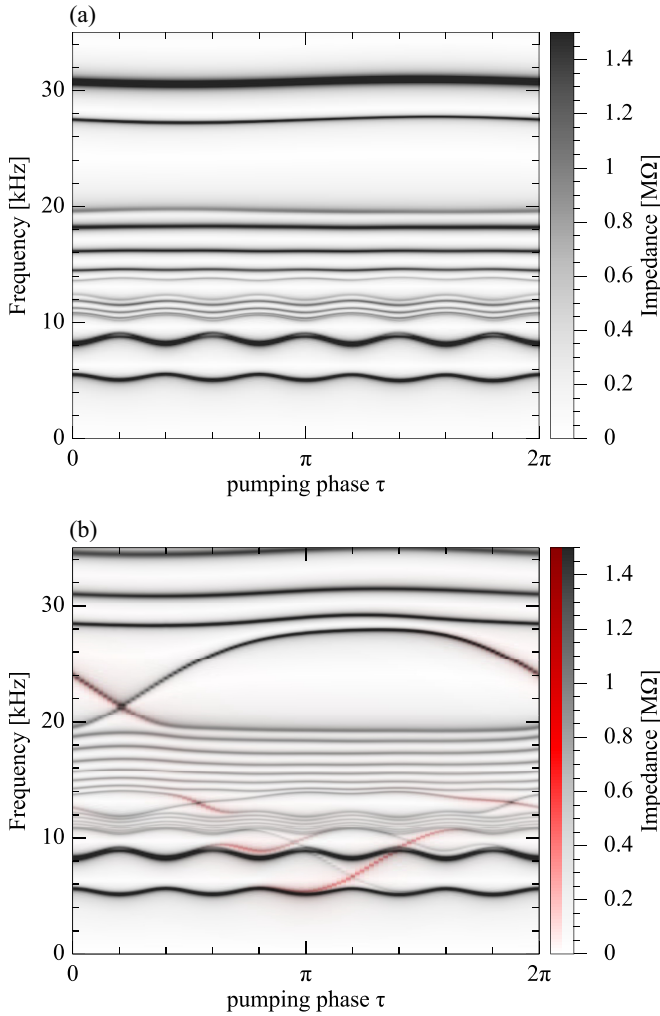


FIG. 2. Measured eigenfrequency band structures. Shown is the sum of impedances from each node to ground (absolute value) for (a) periodic and (b) open boundary conditions, resolved over frequency and pumping phase. Eigenfrequencies appear as peaks in the impedance. The dark lines form eigenfrequency bands over pumping phase τ . In (b), topological edge states emerge that cross the gaps of the band structure. The impedance of the leftmost node to ground is overlaid in red, identifying edge modes localized at the left boundary.

Physically, the matrix elements of the Green function $G_{nm}(\omega)$ are the impedances between nodes n and m , where a diagonal element $G_{nn}(\omega)$ denotes the impedance from node n to ground. To measure them, we record impedance sweeps with frequencies $f = \omega/2\pi$ in the range of 0 to 35 kHz, for different values of τ between 0 and 2π . Since resonances of a circuit are poles (undamped circuit) or peaks (damped circuit) in an eigenvalue $g_i(\omega)$ of $G(\omega)$, we can detect them in the trace of the Green function $\text{tr}[G(\omega)] = \sum_i g_i(\omega)$. Its value is obtained by summing the measured impedances to ground of all nodes.

Figure 2(a) shows the measured trace of the Green function for periodic boundary conditions. Since the circuit consists of eight unit cells of five nodes each, we expect to observe five bands, each containing eight states of different momenta. The five bands can be seen in Fig. 2(a), with the first band within the range of 5–6 kHz, second at 8–9 kHz, third at 10–13 kHz,

fourth at 13–20 kHz, and the fifth band above 27 kHz. The visible subbands correspond to the states of different lattice momentum k . In an L - C circuit, ac currents at low frequency flow predominantly through the inductive components, at high frequencies mostly through the capacitive ones. This is reflected in the observed band structure: The small spread within the low-frequency bands indicates a dominance of the on-site potential, realized by inductors, over the hopping terms realized by capacitors. At the same time, an oscillation of the band as a function of τ can be seen. For high-frequency bands, this observation is reversed, with large spread between modes of differing k but diminished oscillation in τ , indicating a dominance of the capacitive hopping term. A comparison with the theoretical spectrum can be found in the Appendix B.

We also investigate the case of open boundary conditions. Here, dangling capacitors at the end of the chain are connected to ground. The result of the open boundaries impedance measurements is shown in Fig. 2(b). We observe the presence of edge states crossing the band gaps. The Chern numbers of the band can be determined by counting the edge states attached to each band [57]. The winding number ν_n of the gap between bands n and $n + 1$ is the number of ascending minus descending edge modes localized at the left boundary. We obtain winding numbers $\nu_1 = 1$, $\nu_2 = 2$, $\nu_3 = -2$, and $\nu_4 = -1$ by counting the left edge modes marked red in Fig. 2(b). The Chern number of each band is then the difference of winding numbers in the gap above and below $C_n = \nu_n - \nu_{n-1}$. For the five bands we obtain $\{1, 1, -4, 1, 1\}$, which agrees with numerical calculations. The Chern number can also be measured from the shift in the center of mass of a pulse over one pumping period, with the same result for the lowest band as described below.

IV. TOPOLOGICAL PUMPING

We investigate the topological pumping of a signal pulse in a setup with periodic boundaries. To induce pumping, the parameter τ is modulated over time as $\tau(t) = \Omega t$ by applying oscillating control voltages $V_c(t)$. Adiabatic evolution occurs if the pumping frequency Ω is small compared to the resonance frequencies of the circuit. As the adiabatic theorem is most commonly discussed in the quantum-mechanical context of the Schrödinger equation, we provide an analytical derivation for L - C circuits in the Appendix A. We find that the adiabatic theorem still holds but is modified by a rescaling of voltages by the factor $\sqrt{\omega_n(0)/\omega_n(\tau)}$ depending on the resonance frequencies of the respective eigenmodes, which coincides with results previously derived for elastic materials [58]. The effect of temporal modulation can be understood as parallel transport of the instantaneous eigenstates along τ in parameter space. In order to stabilize the signal over long times, a subcircuit compensating parasitic serial resistance is added to the time-dependent inductor, detailed in the Appendix. The topological adiabatic pump transports the wave function of a filled band with Chern number C_n by C_n unit cells per pumping cycle.

In the fermionic Thouless pump, quantized pumping of bulk states relies on the notion of a filled band. We find that for classical systems, we can instead use a signal that is evenly distributed over all states of the given band. For this,

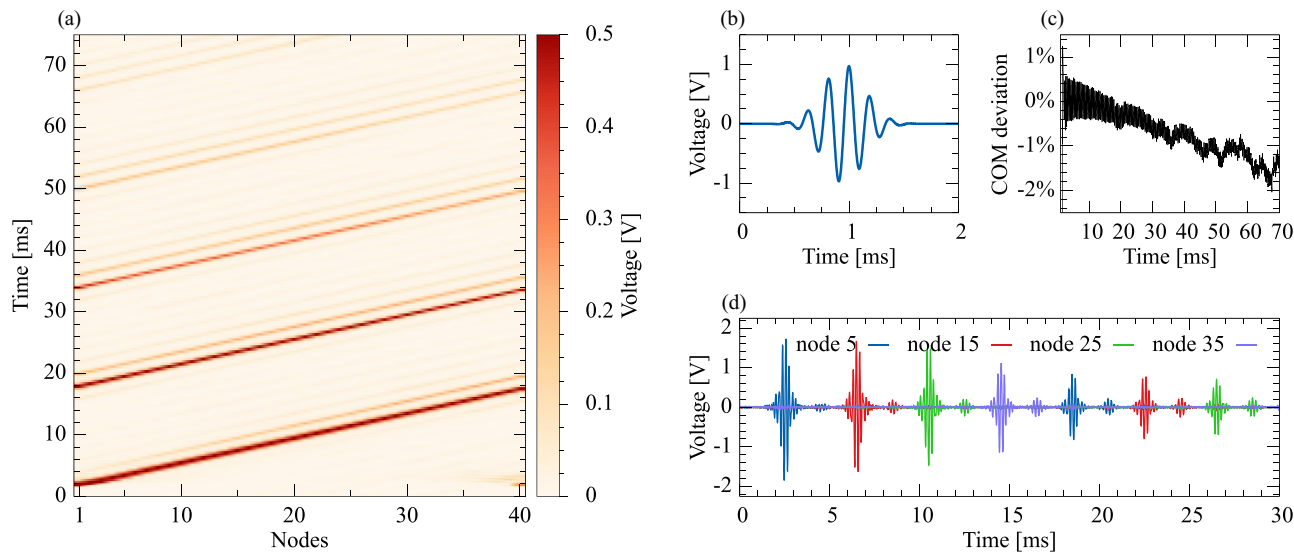


FIG. 3. Adiabatic transport in the bulk for periodic boundaries. (a) Evolution of the voltage pulse over time. The plot shows the signal envelope extracted from measurement data using the Hilbert transform. The pumping potential shifts with a constant velocity of 2.5 nodes/ms. The pulse is well localized in a minimum of the potential and propagates with a velocity proportional to the Chern number of the lowest band. (b) Pulse used to excite the circuit for the bulk transport measurement. Its mean frequency is 5.25 kHz, corresponding to the lowest set of bands in Fig. 3. (c) Relative deviation of the center of mass of the signal from the theoretical trajectory of adiabatic pumping. (d) Voltage evolution over time for selected nodes. Some signal amplitude is observed to tunnel to the following potential minimum with each pass.

we evenly excite the states of the lowest resonance band at a fixed frequency. An exciting current is necessarily distributed evenly in k if fully local in the lattice. At the low frequencies of the first band, hopping term $\frac{d^2}{dt^2}\Gamma_{nm}$ of the equation of motion Eq. (2) is suppressed, so that the on-site term $\Lambda_{nm}(\tau)$ dominates. This means that the induced voltage signal will also be strongly localized and thus approximately uniform in k . This emulates a filled band in that the state has even weight over momentum k , resulting in a quantized pumping velocity [59]. A detailed evaluation of this approximation can be found in the Appendix A. Due to the absence of the Pauli exclusion principle, intraband transitions can occur and cause the breakdown of this analogy. These are suppressed however if the bandwidth is much smaller than the pumping frequency, which is the case for the lowest band in our setup (theory value $\approx 5\text{--}15$ Hz, too small to discern in our measurements).

We inject an ac pulse [see Fig. 3(b)] with mean frequency $f = 5.25$ kHz at node 1, exciting the lowest band of the circuit. The pulse is timed with the minimum of the potential at the injection node to maximize the overlap with the eigenstates of the lowest band. The variable inductors of the circuit are driven at pumping frequency $\Omega = 500$ Hz, moving the potential across the five sites of a unit cell within one period. Accordingly, the adiabatic pumping velocity in the n th band is $C_n \times 500 \text{ Hz} \times 5 \text{ nodes} = C_n \times 2.5 \text{ nodes/ms}$, so it takes $16 \text{ ms}/C_n$ to traverse all 40 nodes of the circuit.

We then measure the evolution of the voltage signal in the circuit. Figure 3(a) shows a density plot of the signal envelope over space (circuit nodes) and time. The signal envelope was extracted from the measurement data using the Hilbert transform as the absolute value of the analytic signal. We observe that the signal is transported across the circuit chain, remaining localized in the potential minimum as it moves along the chain. Figure 3(d) displays the signal over time at different

nodes. We observe that the voltage of the pulse only decays to roughly half of its amplitude after traversing the entire chain once (i.e., 40 nodes or eight unit cells). We also observe some broadening of the pulse, tunneling into neighboring minima of the potential, preferentially the trailing ones. This effect can be best explained as a deviation from the adiabatic approximation, i.e., intra- and interband transitions induced by the drive, since dispersive effects would cause symmetric spreading with no preferred direction. Figure 3(c) shows the relative deviation of the center of mass of the voltage pulse from the trajectory predicted by the Chern number of the lowest band $C_1 = 1$ and pumping frequency $\Omega = 500$ Hz. The graph shows an excellent agreement between theory and experiment, with a relative deviation after 70 ms of less than 2%. This time scale corresponds to the pulse being transported across the entire chain four times. This minimal relative deviation and the small attenuation in space and time suggest the potential of electric circuits to implement very efficient topological adiabatic pumps.

V. CONCLUSION

We show the experimental implementation of a topological adiabatic temporal pump induced by a parameter in the 1D electric circuit. Previous implementations on different platforms face considerable limitations, where deviations in the center of mass of the pulse become significant even after a few pumping periods for small unit cells and system sizes. We illustrate how a quantized transport of voltage pulses in our circuit persists for time scales that are several times the pumping period, which is much longer than in previous realizations. We also quantify the small attenuation in the center of mass of the pulse. Moreover, the distance between circuit nodes in the system is immaterial and not related to any physical length

scale; hence the entire implementation can be miniaturized or expanded significantly. The propagation velocity of the pulse with respect to other parametric variations can likewise be efficiently controlled. Such flexibility and easy implementation with inexpensive components highlight the potential for practical applications, where the physical length and time scales would then be matched to the problem at hand. Furthermore, using our approach to implementing Floquet dynamics in an electric circuit, a large variety of time-periodic phenomena could be studied and realized in this versatile platform, which may be unattainable in other metamaterials.

ACKNOWLEDGMENTS

The work is funded by Deutsche Forschungsgemeinschaft Project No. 258499086 SFB 1170 and through Würzburg-Dresden Cluster of Excellence on Complexity and Topology in Quantum Matter Project No. 390858490 EXC 2147. T.H. was supported by a Ph.D. scholarship of the German Academic Scholarship Foundation. I.B. acknowledges support

from the University of Alberta startup fund UOFAB Startup Boettcher and Natural Sciences and Engineering Research Council of Canada Discovery Grants No. RGPIN-2021-02534 and No. DGECR2021-00043. L.K.U. acknowledges support from SNF Grant No. 13947622-FP476/22Zilberberg.

APPENDIX A: THEORY

1. Topology of the Aubry-André-Harper model

The AAH model is a 1D hopping chain with a cosine-shaped, modulated on-site potential. Its Hamiltonian takes the form

$$H(\tau) = \frac{1}{2} \sum_i (-t c_i^\dagger c_{i+1} + \lambda \cos(\tau - i\varphi) c_i^\dagger c_i + \text{H.c.}). \quad (\text{A1})$$

The potential is shifted by a phase φ between neighboring nodes. If φ is a fraction of 2π , $\varphi = 2\pi/N$, then the model forms a lattice with a periodicity of N sites. The corresponding Bloch Hamiltonian is

$$h(k, \tau) = \begin{pmatrix} \lambda \cos(\tau) & -t & \dots & -t e^{-ik} \\ -t & \lambda \cos(\tau - 2\pi/N) & -t & \vdots \\ \vdots & \vdots & \ddots & -t \\ -t e^{ik} & \dots & -t & \lambda \cos[\tau - 2\pi(N-1)/N] \end{pmatrix}. \quad (\text{A2})$$

We consider the dynamics of an initially localized state in the n th band under adiabatic variation of τ . In this scenario, the AAH model acts as a Thouless pump, transporting the state by C_n unit cells, with C_n the Chern number of the n th band over to the two-dimensional parameter space spanned by lattice momentum k and pumping phase τ . The AAH model is invariant under a combined translation of one site and a shift in the pumping phase τ by φ . Semiclassically, it can be argued that states bound to the minima (or maxima) of the pumping potential should be transported by one unit cell per pumping period, yielding a Chern number of 1 for the corresponding bands. This argument can be formalized by investigating the Berry curvature over the $\{k, \tau\}$ parameter space. The Chern number of the n th band is given by the integral of the Berry curvature:

$$C_n = \frac{1}{2\pi i} \iint dk d\tau [\partial_\tau (\psi_n^\dagger \partial_k \psi_n) - \partial_k (\psi_n^\dagger \partial_\tau \psi_n)], \quad (\text{A3})$$

with $\psi_n(k, \tau)$ being the n th eigenvector of $h(k, \tau)$. Let us investigate the first term of the integral, $\partial_\tau \psi_n^\dagger \partial_k \psi_n$. Assuming a smooth gauge can be chosen within the stripes $0 \leq k < 2\pi$, $(i-1)\varphi \leq \tau < i\varphi$, it can be rewritten as

$$\begin{aligned} & \iint dk d\tau \partial_\tau (\psi_n^\dagger \partial_k \psi_n) \\ &= \int dk ([\psi_n^\dagger \partial_k \psi_n]_{\tau=0}^\varphi + [\psi_n^\dagger \partial_k \psi_n]_{\tau=\varphi}^{2\varphi} \\ & \quad + \dots + [\psi_n^\dagger \partial_k \psi_n]_{\tau=2\pi-\varphi}^{2\pi}) \end{aligned} \quad (\text{A4})$$

$$= \sum_{i=1}^N \int dk [\psi_n^\dagger \partial_k \psi_n]_{\tau=(i-1)\varphi}^{i\varphi}. \quad (\text{A5})$$

Let the eigenvector $\psi_n(k, \tau)$ at $\tau = 0$ be $\psi_n(k, 0) = (a_1, a_2, \dots, a_N)^\top$. At $\tau = \varphi$, the Hamiltonian is shifted by one site compared to $\tau = 0$. Accordingly, the eigenvectors become $\psi_n(k, \varphi) = (e^{ik} a_N, a_1, a_2, \dots, a_{N-1})^\top$. Generally, the eigenvectors for $\tau = i\varphi$ are $\psi_n(k, i\varphi) = (e^{ik} a_{N-i+1}, \dots, e^{ik} a_N, a_1, \dots, a_{N-i})^\top$. Substituting back to the integral, we obtain

$$\begin{aligned} & \sum_{i=1}^N \int dk [\psi_n^\dagger \partial_k \psi_n]_{\tau=(i-1)\varphi}^{i\varphi} \\ &= \sum_{i=1}^N \int dk [\psi_n^\dagger(k, i\varphi) \partial_k \psi_n(k, i\varphi) \\ & \quad - \psi_n^\dagger(k, (i-1)\varphi) \partial_k \psi_n(k, (i-1)\varphi)] \end{aligned} \quad (\text{A6})$$

$$= \sum_i \int dk i |a_i|^2 \quad (\text{A7})$$

$$= \int_0^{2\pi} dk i = 2\pi i. \quad (\text{A8})$$

This term contributes +1 to the Chern number of the respective band. While this calculation does not generate a definitive Chern number for any band, since the second term of the Berry curvature was neglected and assumptions about the smoothness of the gauge need to be made, it shows how the shifting potential biases the bands of the AAH model towards a Chern number of 1. For a finite number of bands, the total Chern number of a system is necessarily zero, so some bands must always violate this result to compensate, i.e.,

there must always be some left-moving modes compensating the right-moving ones.

Another feature that makes the AAH model well suited for the demonstration of topological pumping is the strong localization of low-energy modes. For sufficiently small φ , these essentially correspond to bound states in the wells of the cosine potential that are only weakly coupled to neighboring wells. As a result, low-energy bands are relatively flat, so that a pulse can stay localized over many pumping cycles.

2. Topological states as resonances of an L - C network

The nodal voltages of an L - C network are described by the system of second-order differential equations

$$\Gamma \frac{d^2}{dt^2} \mathbf{V}(t) + \Lambda \mathbf{V}(t) = \frac{d}{dt} \mathbf{I}(t), \quad (\text{A9})$$

where \mathbf{V} is the vector of nodal voltages and \mathbf{I} is the vector of all external currents flowing into the nodes. Γ and Λ are the admittance matrices corresponding to the capacitive and inductive circuit elements respectively. In the frequency domain, the according equation is

$$(-\omega^2 \Gamma + \Lambda) \mathbf{V}(\omega) = i\omega \mathbf{J}(\omega) \mathbf{V}(\omega) = \mathbf{I}(\omega), \quad (\text{A10})$$

where $J(\omega)$ we call the circuit Laplacian. We use this picture of the circuit Laplacian to relate the properties of the quantum-mechanical system to the electrical one, by analogy between J and Hamiltonian H [33]. To calculate the eigenmodes and eigenfrequencies of a circuit, we consider the homogeneous case $\mathbf{I} = \mathbf{0}$ and use an exponential ansatz for the eigenmodes $\mathbf{V}_n(t) = e^{i\omega_n t} \mathbf{V}_n$ to obtain the equation

$$(\Gamma^{-1} \Lambda) \mathbf{V}_n = \omega_n^2 \mathbf{V}_n. \quad (\text{A11})$$

While this approach provides an efficient way to calculate the eigenmodes of the circuit, it does not explain how dynamical eigenstates of the circuit and of the quantum-mechanical Hamiltonian relate. For this, another equivalent defining relation for eigenmodes can be used:

$$J(\omega_n) \mathbf{V}_n = \mathbf{0}. \quad (\text{A12})$$

This relation shows that dynamical modes emerge from the spectrum and eigenvectors of the circuit Laplacian $J(\omega)$ are the eigenpairs at the roots of the admittance eigenvalues $j_n(\omega)$. Consider a set of eigenvectors $\{\mathbf{V}_n(k, \omega(k)) \mid k \in [0, 2\pi[\}$ of the Laplacian of a lattice model. The states of the admittance band at some frequency ω can be recovered by setting $\omega(k) = \omega$, while the states of the eigenfrequency band are obtained by setting $\omega(k)$ to the dispersion relation $\omega_n(k)$. This implies that, if no band crossing occurs in the admittance band structure within the bandwidth of $\omega_n(k)$, the admittance eigenmodes of the Laplacian fixed frequency can be related to the eigenfrequency band structure by a continuous deformation. Accordingly, the band topology of the dynamical eigenstates is equivalent to that of the corresponding admittance eigenstates at a suitably chosen frequency ω_0 , which themselves are analogous to that of the respective Hamiltonian H after which $J(\omega_0)$ was modeled.

3. Adiabatic evolution in a modulated L - C electric circuit

To rederive the adiabatic theorem for an L - C circuit, we first reexpress the differential equation of the circuit in the canonical form

$$i \frac{d}{dt} \begin{pmatrix} \dot{\mathbf{V}} \\ \mathbf{V} \end{pmatrix} = i \begin{pmatrix} 0 & -\Gamma^{-1} \Lambda \\ \mathbb{1} & 0 \end{pmatrix} \begin{pmatrix} \dot{\mathbf{V}} \\ \mathbf{V} \end{pmatrix}. \quad (\text{A13})$$

This differential equation is equivalent to a non-Hermitian Schrödinger equation with

$$H = i \begin{pmatrix} 0 & -\Gamma^{-1} \Lambda \\ \mathbb{1} & 0 \end{pmatrix}. \quad (\text{A14})$$

The matrix $\Gamma^{-1} \Lambda$ has eigenvalues and eigenvectors ω_n^2 and \mathbf{V}_n , so $\Gamma^{-1} \Lambda \mathbf{V}_n = \omega_n^2 \mathbf{V}_n$. In the context of an L - C circuit with positive, reciprocal capacitive and inductive couplings (such as any circuit composed of conventional passive elements), the matrices Γ and Λ are real-valued, symmetric, positive semidefinite, and diagonally dominant, so their eigenvalues are real and positive. Since Γ is symmetric with positive eigenvalues, so is Γ^{-1} . The product $\Gamma^{-1} \Lambda$ on the other hand is generally not symmetric, since the two factor matrices generally do not commute. However, direct calculation shows that it remains positive (semi)definite, so all its eigenvalues are real and positive. This implies their square roots $\pm\omega_n$ are real valued as well. The eigenvectors to $(\Gamma^{-1} \Lambda)^\top = \Lambda \Gamma^{-1}$ form the set of left eigenvectors \mathbf{W}_n that form a dual basis with the \mathbf{V}_n , so that $\mathbf{W}_n^\top \mathbf{V}_m = \delta_{nm}$.

A set of eigenvectors $\Psi_{n\sigma}$ to H , with $\sigma \in \{+, -\}$ and eigenvalues $\omega_{n\sigma} = \sigma \omega_n$ (where we choose $+\omega_n$ to always be the positive root of the corresponding eigenvalue of $\Gamma^{-1} \Lambda$), can be constructed from the \mathbf{V}_n as

$$\Psi_{n\sigma} = \begin{pmatrix} -\sigma i \omega_n \mathbf{V}_n \\ \mathbf{V}_n \end{pmatrix}. \quad (\text{A15})$$

The left eigenvectors of H are given by

$$\Phi_{n\sigma} = \frac{1}{2\sigma i \omega_n} \begin{pmatrix} \mathbf{W}_n \\ \sigma i \omega_n \mathbf{W}_n \end{pmatrix}. \quad (\text{A16})$$

A quick calculation confirms that these form the dual basis to $\Psi_{n\sigma}$, namely,

$$\Phi_{m\rho}^\dagger \Psi_{n\sigma} = \frac{1}{-2\sigma i \omega_n} (\mathbf{W}_m^\dagger, -\rho i \omega_m \mathbf{W}_m^\dagger) \begin{pmatrix} -\sigma i \omega_n \mathbf{V}_n \\ \mathbf{V}_n \end{pmatrix} \quad (\text{A17})$$

$$= \frac{1}{-2\sigma i \omega_n} (-\sigma i \omega_n \delta_{mn} - \rho i \omega_m \delta_{mn}) \quad (\text{A18})$$

$$= \frac{-\sigma i \omega_n}{-2\sigma i \omega_n} (1 + \rho \sigma) \delta_{mn} \quad (\text{A19})$$

$$= \delta_{\rho\sigma} \delta_{mn}. \quad (\text{A20})$$

A general state of the circuit is described as a linear combination of the eigenstates $\Psi(t) = \sum_{n\sigma} c_{n\sigma}(t) \Psi_{n\sigma}(t)$. From the reality constraint of \mathbf{V} and $\dot{\mathbf{V}}$, we obtain that the coefficients corresponding to the same n must be complex conjugates of each other, $c_{n-} = c_{n+}^*$. The voltages of the system are then simply the second component of $\Psi(t)$, so that $\mathbf{V}(t) = \sum_{n\sigma} c_{n\sigma}(t) \mathbf{V}_n(t)$. Using these conventions, we can use the same set of coefficients $c_{n\sigma}$ to describe both the state vector Ψ and voltage vector \mathbf{V} of the system. To derive the adiabatic

theorem for slowly modulated L - C circuits, we start from the Schrödinger equation projected onto a left eigenstate and simplify from there. We have

$$\Phi_{m\rho}^\dagger H \sum_{n\sigma} c_{n\sigma} \Psi_{n\sigma} = \Phi_{m\rho}^\dagger i \frac{d}{dt} \sum_{n\sigma} c_{n\sigma} \Psi_{n\sigma}, \quad (\text{A21})$$

$$\Phi_{m\rho}^\dagger \sum_{n\sigma} \sigma \omega_n c_{n\sigma} \Psi_{n\sigma} = i \Phi_{m\rho}^\dagger \sum_{n\sigma} (\dot{c}_{n\sigma} \Psi_{n\sigma} + c_{n\sigma} \dot{\Psi}_{n\sigma}), \quad (\text{A22})$$

$$\rho \omega_m c_{m\rho} = i \dot{c}_{m\rho} + i \sum_{n\sigma} c_{n\sigma} \Phi_{m\rho}^\dagger \dot{\Psi}_{n\sigma} \quad (\text{A23})$$

$$= i \dot{c}_{m\rho} + i \sum_{n\sigma} c_{n\sigma} \frac{1}{-2\rho i \omega_m} (\mathbf{W}_m^\dagger, -\rho i \omega_m \mathbf{W}_m^\dagger) \begin{pmatrix} -\sigma i (\dot{\omega}_n \mathbf{V}_n + \omega_n \dot{\mathbf{V}}_n) \\ \dot{\mathbf{V}}_n \end{pmatrix} \quad (\text{A24})$$

$$= i \dot{c}_{m\rho} + i \sum_{n\sigma} c_{n\sigma} \frac{1}{-2\rho i \omega_m} (-\sigma i \dot{\omega}_n \delta_{mn} - \sigma i \omega_n \mathbf{W}_m^\dagger \dot{\mathbf{V}}_n - \rho i \omega_m \mathbf{W}_m^\dagger \dot{\mathbf{V}}_n) \quad (\text{A25})$$

$$= i \dot{c}_{m\rho} + i \sum_{n\sigma} c_{n\sigma} \frac{1}{2} \left[\sigma \rho \frac{\dot{\omega}_n}{\omega_m} \delta_{mn} + \left(\sigma \rho \frac{\omega_n}{\omega_m} + 1 \right) \mathbf{W}_m^\dagger \dot{\mathbf{V}}_n \right] \quad (\text{A26})$$

$$= i \dot{c}_{m\rho} + i \rho \frac{\dot{\omega}_m}{\omega_m} \frac{c_{m+} - c_{m-}}{2} + i \sum_{n\sigma} c_{n\sigma} \frac{1}{2} \left(\rho \sigma \frac{\omega_n}{\omega_m} + 1 \right) \mathbf{W}_m^\dagger \dot{\mathbf{V}}_n \quad (\text{A27})$$

$$= i \dot{c}_{m\rho} - \frac{\dot{\omega}_m}{\omega_m} \text{Im} c_{m+} + i c_{m\rho} \mathbf{W}_m^\dagger \dot{\mathbf{V}}_m + i \sum_{n \neq m\sigma} c_{n\sigma} \frac{1}{2} \left(\rho \sigma \frac{\omega_n}{\omega_m} + 1 \right) \mathbf{W}_m^\dagger \dot{\mathbf{V}}_n \quad (\text{A28})$$

$$= i \dot{c}_{m\rho} - \frac{\dot{\omega}_m}{\omega_m} \text{Im} c_{m+} + i c_{m\rho} \mathbf{W}_m^\dagger \dot{\mathbf{V}}_m + i \sum_{n \neq m\sigma} c_{n\sigma} \frac{1}{2} \left[1 + \rho \sigma + \rho \sigma \left(\frac{\omega_n}{\omega_m} - 1 \right) \right] \mathbf{W}_m^\dagger \dot{\mathbf{V}}_n \quad (\text{A29})$$

$$= i \dot{c}_{m\rho} - \frac{\dot{\omega}_m}{\omega_m} \text{Im} c_{m+} + i c_{m\rho} \mathbf{W}_m^\dagger \dot{\mathbf{V}}_m + i \sum_{n \neq m} c_{n\rho} \mathbf{W}_m^\dagger \dot{\mathbf{V}}_n - \sum_{n \neq m} \rho \text{Im} c_{n+} \left(\frac{\omega_n}{\omega_m} - 1 \right) \mathbf{W}_m^\dagger \dot{\mathbf{V}}_n. \quad (\text{A30})$$

We arrive at

$$\dot{c}_{m\rho} + (i\rho\omega_m + \mathbf{W}_m^\dagger \dot{\mathbf{V}}_m) c_{m\rho} = - \sum_{n \neq m} c_{n\rho} \mathbf{W}_m^\dagger \dot{\mathbf{V}}_n - i \sum_n \text{Im} c_{n+} \left[\frac{\dot{\omega}_m}{\omega_m} \delta_{nm} + \rho \left(\frac{\omega_n}{\omega_m} - 1 \right) \mathbf{W}_m^\dagger \dot{\mathbf{V}}_n \right]. \quad (\text{A31})$$

This can be simplified further by setting $\rho = +1$, removing the redundant negative frequency case that is related to the positive frequency coefficients by complex conjugation. Suppressing the now redundant second index, the equation then reads

$$\dot{c}_m + (i\omega_m + \mathbf{W}_m^\dagger \dot{\mathbf{V}}_m) c_m = - \sum_{n \neq m} c_n \mathbf{W}_m^\dagger \dot{\mathbf{V}}_n - i \sum_n \text{Im} c_n \left[\frac{\dot{\omega}_m}{\omega_m} \delta_{nm} + \left(\frac{\omega_n}{\omega_m} - 1 \right) \mathbf{W}_m^\dagger \dot{\mathbf{V}}_n \right]. \quad (\text{A32})$$

The terms on the left-hand side correspond to the dynamical evolution of the quasistatic eigenstates and the geometric component of the transport that results in the Berry phase, identical to the known quantum-mechanical case. On the right-hand side of the equation, the first term is analogous to the quantum-mechanical case (and neglected in the conventional adiabatic approximation). However, an additional term proportional to the imaginary part of the coefficients c_n appears. To investigate which of these terms can be neglected under adiabatic evolution, we substitute the coefficients $c_n(t)$ by $e^{-i \int^t \omega_n(t') dt'} \tilde{c}_n(t)$. This cancels the dynamical term $i\omega_n c_n$ on the left-hand side of Eq. (A32) and after multiplying the equation by $e^{i \int^t \omega_m(t') dt'}$ we obtain

$$\dot{\tilde{c}}_m + \mathbf{W}_m^\dagger \dot{\mathbf{V}}_m \tilde{c}_m = - \sum_{n \neq m} e^{-i \int^t (\omega_n - \omega_m) dt'} \tilde{c}_n \mathbf{W}_m^\dagger \dot{\mathbf{V}}_n - i \sum_n \text{Im} e^{-i \int^t \omega_n dt'} \tilde{c}_n e^{i \int^t \omega_m dt'} \left[\frac{\dot{\omega}_m}{\omega_m} \delta_{nm} + \left(\frac{\omega_n}{\omega_m} - 1 \right) \mathbf{W}_m^\dagger \dot{\mathbf{V}}_n \right] \quad (\text{A33})$$

$$= - \sum_{n \neq m} e^{-i \int^t (\omega_n - \omega_m) dt'} \tilde{c}_n \mathbf{W}_m^\dagger \dot{\mathbf{V}}_n - \sum_n \frac{e^{-i \int^t (\omega_n - \omega_m) dt'} \tilde{c}_n - e^{i \int^t (\omega_n + \omega_m) dt'} \tilde{c}_n^*}{2} \left[\frac{\dot{\omega}_m}{\omega_m} \delta_{nm} + \left(\frac{\omega_n}{\omega_m} - 1 \right) \mathbf{W}_m^\dagger \dot{\mathbf{V}}_n \right]. \quad (\text{A34})$$

We see that all terms with $n \neq m$ on the right side oscillate with a finite frequency. If adiabatic evolution is assumed, these terms vanish since their contribution to $c(\tau)$ is of order $\Omega/(\omega_n - \omega_m)$. Only one of the right-hand side terms remains:

$$\dot{\tilde{c}}_m + \mathbf{W}_m^\dagger \dot{\mathbf{V}}_m \tilde{c}_m = - \frac{1}{2} \frac{\dot{\omega}_m}{\omega_m} \tilde{c}_m \quad (\text{A35})$$

$$\iff \dot{\tilde{c}}_m = -(\mathbf{W}_m^\dagger \dot{\mathbf{V}}_m + \omega_m^{-1} \dot{\omega}_m / 2) \tilde{c}_m. \quad (\text{A36})$$

The term $\mathbf{W}_m^\dagger \dot{\mathbf{V}}_m$ is the Berry phase of a non-Hermitian system, analogous to the quantum-mechanical case of a non-Hermitian Hamiltonian. The other term $\omega_m^{-1} \dot{\omega}_m/2$ has no direct analog in quantum mechanics. Both these terms induce a purely geometric evolution in parameter space along the curve $C : [t_0, t] \rightarrow \mathbb{R}^N$, parametrized by $\mathbf{R}(t)$, via

$$\dot{\tilde{c}}_m = (\nabla_R c_m) \frac{d\mathbf{R}}{dt} = -(\mathbf{W}_m^\dagger \nabla_R \mathbf{V}_m + \omega_m^{-1} \nabla_R \omega_m/2) \frac{d\mathbf{R}}{dt} \tilde{c}_m, \quad (\text{A37})$$

$$\nabla_R \tilde{c}_m = -(\mathbf{W}_m^\dagger \nabla_R \mathbf{V}_m + \omega_m^{-1} \nabla_R \omega_m/2) \tilde{c}_m, \quad (\text{A38})$$

$$\Rightarrow \tilde{c}_m(\mathbf{R}) = \exp \left[\int_C -(\mathbf{W}_m^\dagger \nabla_R \mathbf{V}_m + \omega_m^{-1} \nabla_R \omega_m/2) d\mathbf{R} \right] \tilde{c}_m(\mathbf{R}_0) \quad (\text{A39})$$

$$= \exp \left[\int_C -\mathbf{W}_m^\dagger \nabla_R \mathbf{V}_m d\mathbf{R} - \ln \left(\frac{\omega_m(\mathbf{R})}{\omega_m(\mathbf{R}_0)} \right) / 2 \right] \tilde{c}_m(\mathbf{R}_0) \quad (\text{A40})$$

$$= \sqrt{\frac{\omega_m(\mathbf{R}_0)}{\omega_m(\mathbf{R})}} e^{i\gamma_m[C]} \tilde{c}_m(\mathbf{R}_0). \quad (\text{A41})$$

Here we see that, ultimately, the difference between adiabatic evolution in quantum mechanics and electrical L - C circuits is a rescaling of the voltage amplitude by $\sqrt{\frac{\omega_m(\mathbf{R}_0)}{\omega_m(\mathbf{R})}}$, the square root of the ratio of initial and final eigenfrequency of the respective state.

APPENDIX B: CIRCUIT SETUP

1. Floquet element with loss compensation

The time variable inductors used in our experimental setup are implemented using AD633 analog multipliers. The multipliers have voltage inputs named X1, X2, Y1, Y2, and Z, and voltage output W . The ideal output voltage is given by

$$W = \frac{(X1 - X2)(Y1 - Y2)}{10V} + Z. \quad (\text{B1})$$

To create the effective variable inductor as shown in Fig. 4, the voltage of the connected node is fed into X1, and control

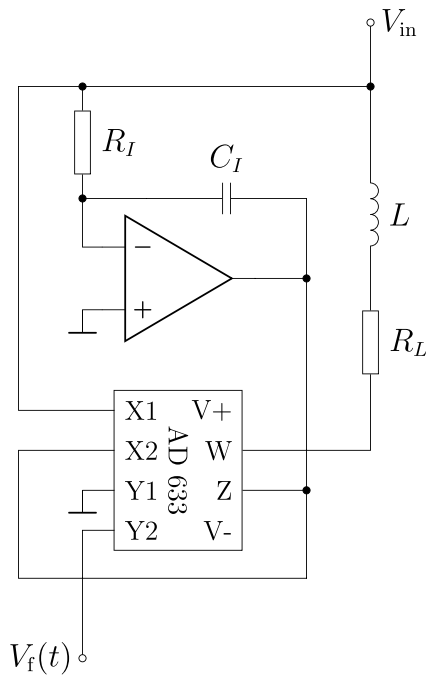


FIG. 4. Floquet inductor including the serial resistance compensation subcircuit. Not shown: Voltage divider at the output of the operational amplifier for fine tuning.

voltage V_f is fed into Y2. Then the voltage across inductor L connected between the connected node and W is $V_{in} + V_{in} \frac{V_f}{10V} = (1 + \frac{V_f}{10V}) V_{in}$. The current through the inductor is then

$$I = \int dt \left(1 + \frac{V_f}{10V} \right) L^{-1} V_{in}. \quad (\text{B2})$$

The op-amp acts as an analog integrator of the input voltage, and its output voltage is given by $-\frac{1}{i\omega R_I C_I} V_{in}$. This signal is fed into the Z and X2 inputs of the analog multipliers, so that it is subtracted from the X1 input before multiplication and added to the output after multiplication. This way, the output W of the analog multiplier is

$$W = \left(V_{in} + \frac{1}{i\omega R_I C_I} V_{in} \right) f(\tau) - \frac{1}{i\omega R_I C_I} V_{in} \quad (\text{B3})$$

$$= V_{in} \left[\left(1 + \frac{1}{i\omega R_I C_I} \right) f(\tau) - \frac{1}{i\omega R_I C_I} \right]. \quad (\text{B4})$$

Finally, the output current flowing from the connected node through inductor L with parasitic serial resistance R_L is

$$I = \frac{V_{in} - W}{i\omega L + R_L} \quad (\text{B5})$$

$$= \frac{1}{i\omega L} \frac{\left(1 + \frac{1}{i\omega R_I C_I} \right) [1 - f(\tau)]}{1 + \frac{R_L}{i\omega L}} V_{in}. \quad (\text{B6})$$

Now R_I and C_I are chosen such that $\frac{1}{R_I C_I} = \frac{R_L}{L}$ and we obtain

$$I = \frac{1}{i\omega L} [1 - f(\tau)] V_{in}. \quad (\text{B7})$$

This means that the added subcircuit can precisely compensate for the serial resistance of the inductor, which we consider to be the main cause of parasitic loss. The influence of the serial resistance of the time varying inductor on the amplitude of the fed-in pulse is shown in Fig. 5. In our setup, an additional voltage divider consisting of two 100-k Ω resistors and a 5-k Ω potentiometer was included to fine tune the output voltage of the integrator subcircuit. The influence of this compensation

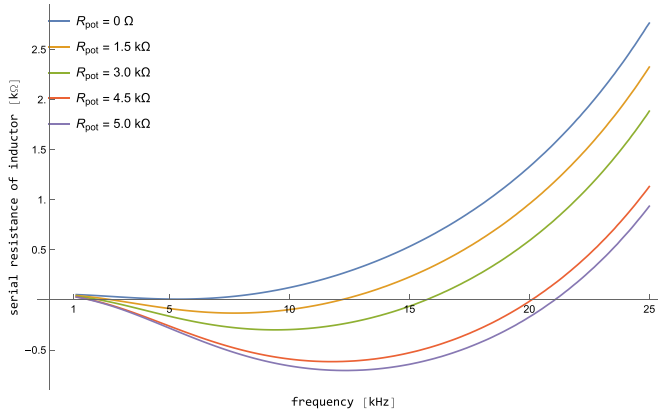


FIG. 5. Influence of tuning the resistance of the potentiometer in the compensation subcircuit [see Fig. 4 and Eq. (B6)] on the serial resistance of the inductor of a single node. For a resistance setting of the potentiometer of slightly above 0Ω the resistance of the inductor gets very close to 0Ω as well, allowing for the injected pulse to survive longer on its way along the circuit chain. Negative resistance values, i.e., overcompensation, at the frequency of the injected pulse result in a gain of the signal and therefore in saturation of the multiplier output, which had to be avoided.

on the serial resistance of the inductor is shown in Fig. 5 for different compensations, i.e., different resistance settings in the potentiometer, over frequency. For a resistance setting of the potentiometer of slightly above 0Ω the resistance of the inductor gets very close to 0Ω as well, allowing for the injected pulse to survive longer on its way along the circuit chain.

2. Emulating a filled band

Quantized transport in the topological Thouless pump requires the band in which pumping is performed to be filled, so that the nonquantized dispersive component of transport vanishes. As mentioned in the main text, we emulate this in our system by equally exciting all states of a band. This way, despite the concept of a filled band being absent in classical

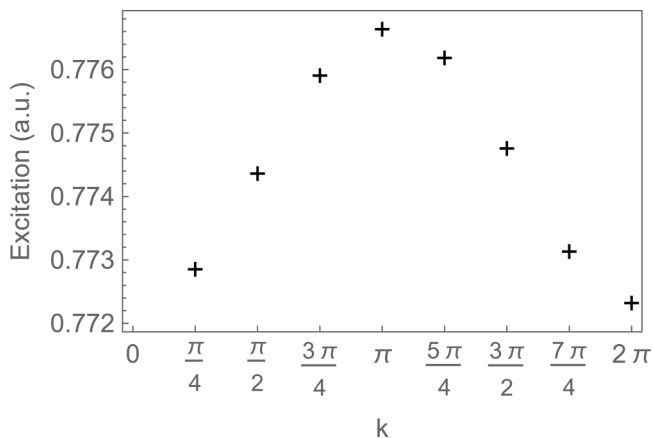


FIG. 6. Simulated relative excitation of the states in the lowest band when excited resonantly by a localized voltage pulse, with pumping phase τ tuned such that the excitation is localized in a potential valley.

metamaterials, we can eliminate dispersive transport, and are left with only adiabatic transport.

As explained in the main text, we approximate a uniform excitation of all states of the lowest band in our circuit model by injecting a local current pulse. In this section, we verify numerically how well this method works in generating an approximately uniform voltage response.

The response of the circuit to an external current signal can be calculated from the circuit Laplacian as

$$\mathbf{V}(k, \omega) = [\mathbf{J}(k, \omega)]^{-1} \mathbf{I}(k, \omega). \quad (\text{B8})$$

Here, use the Bloch representation, with Bloch momentum k taking values $k = 2\pi/8, \dots, 2\pi$ as our circuit consists of eight unit cells. For $\mathbf{J}(k, \omega)$, we use the circuit Laplacian as specified in the main text, but with a parasitic serial resistance of 82Ω added to each inductor, which is the dc resistance of the inductors used in experiment. We calculate the excitation of each state in the lowest band by evaluating (B8) at the resonance frequency of the first band for each respective value of k . The resonances are calculated from the poles of $[\mathbf{J}(k, \omega)]^{-1}$ over $\omega \in \mathbb{C}$, where the resonance frequencies are the real values of the positions of the poles. We take the norm of the obtained voltage response vectors and plot the result over k in Fig. 6. We see that the different momentum states of the band are excited approximately evenly, with a relative spread of less than $\pm 0.5\%$.

3. Effect of disorder on the band structure

In order to gauge the effect of disorder on the resonance band structure, we simulate impedance sweeps of the system. For this, we start with the circuit Laplacian as described in the previous section and add disorder to the contributions of the individual elements making up the circuit. We use the values as specified for the experimental setup of $\pm 1\%$ for the hopping capacitors, $\pm 5\%$ for the inductors to ground. The impedance sweep is calculated by sampling the trace of the inverse of the Laplacian over different values of frequency and pumping phase τ . Figure 7 shows a comparison of the measured impedance sweep [Fig. 7(a)] to a sweep calculated from theory without disorder [Fig. 7(b)] and with disorder [Fig. 7(c)]. A visual comparison shows little deviation between all three figures in the region of the lowest three bands (≈ 0 – 15 kHz). In the region of the upper bands, we observe a significant distortion of the experimental bands compared to the simulated ones. For instance, the lowest state of the fifth band in Fig. 7(a) lies at ≈ 27.5 kHz whereas the same state can be seen at ≈ 31.5 kHz in Figs. 7(b) and 7(c). Furthermore, we observe that the higher bands start bending when disorder is introduced, though the effect is enhanced in the experimental setup [Fig. 7(a)] compared to the simulation with disorder [Fig. 7(c)]. Overall, there is good correspondence between the theoretical and simulated bands and we do not expect the minor observed deviations to be relevant to our experimental measurements of boundary states and topological pumping.

4. Measurement setup and procedure

For our experimental setup we devised printed circuit boards. Our chosen circuit elements are surface mounted capacitors for hopping between nodes, through hole inductors to

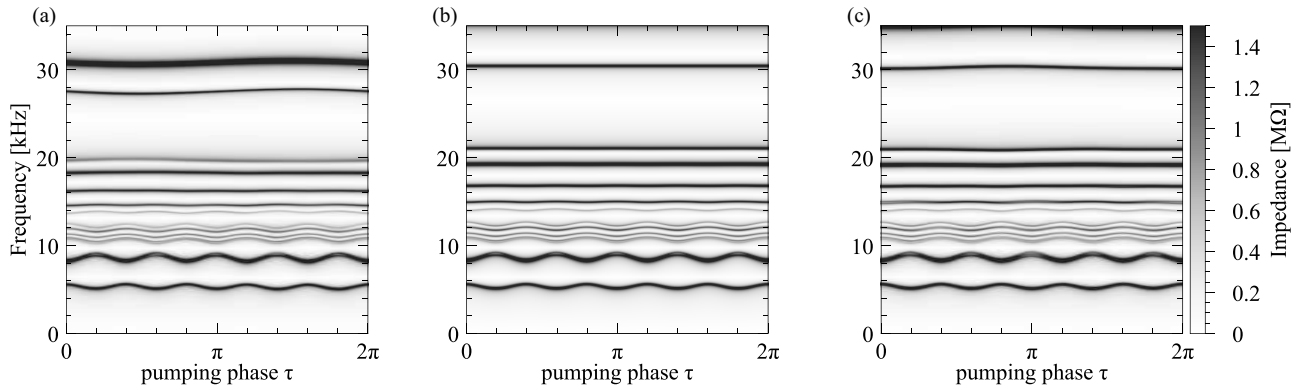


FIG. 7. Comparison of experimental impedance sweep to theory. (a) Measured impedance sweep as shown in the main text. (b) Theoretical impedance sweep for no component disorder. (c) Simulated impedance sweep for nominal component disorder, calculated from an instance of the Laplacian with disorder, assuming uniform distribution of component values in the range of tolerance.

ground, through hole resistors for tuning reasons (see Fig. 8), as well as through one analog multiplier and one operational amplifier per node. The multiplier is used to generate a time dependence in the behavior of the inductor, whereas the operational amplifier is part of an integrator circuit which is used to emulate nearly vanishing serial resistance of the inductor.

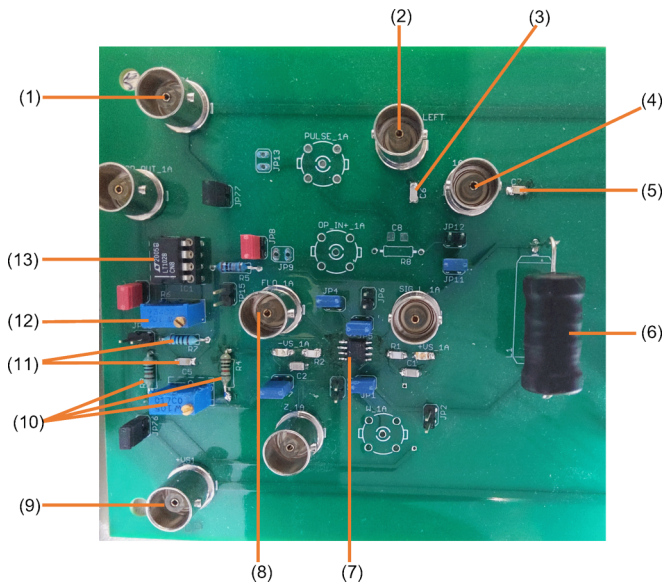


FIG. 8. Single node of the Thouless pump circuit. (1) BNC connector for negative supply voltage. (2) BNC connector to previous board. (3) Hopping capacitor to previous node. (4) BNC connector to measured node. (5) Hopping capacitor to next node. (6) Inductor of measured node. (7) Analog multiplier providing time dependence for the inductor. (8) BNC connector to input Floquet signal into the multiplier. (9) BNC connector for positive supply voltage. (10) Resistors for gain adjustment to minimize serial resistance of the inductor. (11) Resistor and capacitor of the integrator built from the operational amplifier. (12) Potentiometer for offset adjustment of operational amplifier. (13) Operational amplifier used as part of an integrator in combination with the elements of (11).

This integrator was necessary to keep the measured pulses alive long enough to make several turns in the periodic chain. To preserve translational symmetry the scatter of the absolute values of the circuit elements needed to be smaller than typical tolerances of commercially available components. To this end all components were precharacterized by a BK Precision 894 LCR meter. The following choices of components with tolerances after the characterization process and selection were made for this experimental setup. Inductor to ground: Bourns 5900-104-RC nominal values $L = 100 \text{ mH} \pm 5\%$ and $R_{dc} = 82 \Omega \pm 5\%$. Hopping capacitor: Yageo CC0603GR-NPO-8BN102 nominal values $C = 1 \text{ nF} \pm 1\%$. Integrator capacitor: Murata GJM1555-C1H470-GB01D nominal values $C = 47 \text{ pF} \pm 2\%$. Resistor before integrator: Yageo MF0204 $R = 100 \text{ M}\Omega \pm 1\%$. Resistor within integrator: Yageo MF0204 $R = 100 \text{ M}\Omega \pm 1\%$. Resistors within voltage divider: Yageo MF0207 $R = 100 \text{ k}\Omega \pm 0.1\%$. Potentiometer within voltage divider: Bourns PV36-W502-C01B00 $R = 5 \text{ k}\Omega \pm 10\%$. The circuit was excited at the first node with a signal which was of the form $V_0 \sin(ft) \exp(-\frac{t^2}{2\sigma^2})$, a product of a sinusoidal signal at $f = 5.25 \text{ kHz}$ and a Gaussian with a standard deviation of $\sigma = 0.175 \text{ ms}^{-1}$ [see Fig. 3(b)] from an Agilent 33220A arbitrary waveform generator coupled inductively to the inductor of the first node using an inductor of the same kind as used on the board. To reduce the cross talk of the inductors, their respective spots within a node were rotated by 90° from one node to the other. Additionally the inductors were each lifted 3 cm above the board to reduce interaction with the ground plane within the board. This lifting of the inductors showed a significant sharpening of the impedance peaks on each node increasing the measured impedance by a factor of up to 10. The propagating wavefronts were measured with oscilloscopes of the PicoScope 4000 Series by PICOtech, connected to each node. The impedance measurements at each node for the eigenfrequency band structures were performed with an MFIA by Zurich instruments. For this measurement the Floquet phases were chosen stationary with a difference of $2\pi/5$ from one node to the next. The whole 2π of the Floquet phase was then sampled in 100 equidistant points, leading to the figures shown in the main text.

- [1] D. J. Thouless, Quantization of particle transport, *Phys. Rev. B* **27**, 6083 (1983).
- [2] M. Z. Hasan and C. L. Kane, *Colloquium: Topological insulators*, *Rev. Mod. Phys.* **82**, 3045 (2010).
- [3] Q. Niu and D. J. Thouless, Quantised adiabatic charge transport in the presence of substrate disorder and many-body interaction, *J. Phys. A* **17**, 2453 (1984).
- [4] M. Lohse, C. Schweizer, O. Zilberberg, M. Aidelsburger, and I. Bloch, A Thouless quantum pump with ultracold bosonic atoms in an optical superlattice, *Nat. Phys.* **12**, 350 (2016).
- [5] S. Nakajima, T. Tomita, S. Taie, T. Ichinose, H. Ozawa, L. Wang, M. Troyer, and Y. Takahashi, Topological Thouless pumping of ultracold fermions, *Nat. Phys.* **12**, 296 (2016).
- [6] H.-I. Lu, M. Schemmer, L. M. Ayccock, D. Genkina, S. Sugawa, and I. B. Spielman, Geometrical pumping with a Bose-Einstein condensate, *Phys. Rev. Lett.* **116**, 200402 (2016).
- [7] Y. Ke, X. Qin, F. Mei, H. Zhong, Y. S. Kivshar, and C. Lee, Topological phase transitions and Thouless pumping of light in photonic waveguide arrays, *Laser Photon. Rev.* **10**, 995 (2016).
- [8] A. Cerjan, M. Wang, S. Huang, K. P. Chen, and M. C. Rechtsman, Thouless pumping in disordered photonic systems, *Light: Sci. Appl.* **9**, 178 (2020).
- [9] M. Jürgensen, S. Mukherjee, and M. C. Rechtsman, Quantized nonlinear Thouless pumping, *Nature (London)* **596**, 63 (2021).
- [10] Y.-K. Sun, X.-L. Zhang, F. Yu, Z.-N. Tian, Q.-D. Chen, and H.-B. Sun, Non-Abelian Thouless pumping in photonic waveguides, *Nat. Phys.* **18**, 1080 (2022).
- [11] W. Cheng, E. Prodan, and C. Prodan, Experimental demonstration of dynamic topological pumping across incommensurate bilayered acoustic metamaterials, *Phys. Rev. Lett.* **125**, 224301 (2020).
- [12] O. You, S. Liang, B. Xie, W. Gao, W. Ye, J. Zhu, and S. Zhang, Observation of non-Abelian Thouless pump, *Phys. Rev. Lett.* **128**, 244302 (2022).
- [13] I. H. Grinberg, M. Lin, C. Harris, W. A. Benalcazar, C. W. Peterson, T. L. Hughes, and G. Bahl, Robust temporal pumping in a magneto-mechanical topological insulator, *Nat. Commun.* **11**, 974 (2020).
- [14] Y. Xia, E. Riva, M. I. N. Rosa, G. Cazzulani, A. Erturk, F. Braghin, and M. Ruzzene, Experimental observation of temporal pumping in electromechanical waveguides, *Phys. Rev. Lett.* **126**, 095501 (2021).
- [15] Z.-C. Xiang, K. Huang, Y.-R. Zhang, T. Liu, Y.-H. Shi, C.-L. Deng, T. Liu, H. Li, G.-H. Liang, Z.-Y. Mei, H. Yu, G. Xue, Y. Tian, X. Song, Z.-B. Liu, K. Xu, D. Zheng, F. Nori, and H. Fan, Simulating Chern insulators on a superconducting quantum processor, *Nat. Commun.* **14**, 5433 (2023).
- [16] H. Weisbrich, R. L. Klees, O. Zilberberg, and W. Belzig, Fractional transconductance via nonadiabatic topological cooper pair pumping, *Phys. Rev. Res.* **5**, 043045 (2023).
- [17] S. Athanasiou, I. E. Nielsen, M. M. Wauters, and M. Burrello, Thouless pumping in Josephson junction arrays, [arXiv:2308.13597](https://arxiv.org/abs/2308.13597).
- [18] S. Nakajima, N. Takei, K. Sakuma, Y. Kuno, P. Marra, and Y. Takahashi, Competition and interplay between topology and quasi-periodic disorder in Thouless pumping of ultracold atoms, *Nat. Phys.* **17**, 844 (2021).
- [19] J. Minguzzi, Z. Zhu, K. Sandholzer, A.-S. Walter, K. Viebahn, and T. Esslinger, Topological pumping in a Floquet-Bloch band, *Phys. Rev. Lett.* **129**, 053201 (2022).
- [20] K. Viebahn, A.-S. Walter, E. Bertok, Z. Zhu, M. Gächter, A. A. Aligia, F. Heidrich-Meisner, and T. Esslinger, Interaction-induced charge pumping in a topological many-body system, [arXiv:2308.03756](https://arxiv.org/abs/2308.03756).
- [21] J. Tangpanitanon, V. M. Bastidas, S. Al-Assam, P. Roushan, D. Jaksch, and D. G. Angelakis, Topological pumping of photons in nonlinear resonator arrays, *Phys. Rev. Lett.* **117**, 213603 (2016).
- [22] N. Mostaan, F. Grusdt, and N. Goldman, Quantized topological pumping of solitons in nonlinear photonics and ultracold atomic mixtures, *Nat. Commun.* **13**, 5997 (2022).
- [23] M. Jürgensen and M. C. Rechtsman, Chern number governs soliton motion in nonlinear Thouless pumps, *Phys. Rev. Lett.* **128**, 113901 (2022).
- [24] V. Brosco, L. Piloizzi, R. Fazio, and C. Conti, Non-Abelian Thouless pumping in a photonic lattice, *Phys. Rev. A* **103**, 063518 (2021).
- [25] Z. Fedorova, H. Qiu, S. Linden, and J. Kroha, Observation of topological transport quantization by dissipation in fast Thouless pumps, *Nat. Commun.* **11**, 3758 (2020).
- [26] F. Nathan, R. Ge, S. Gazit, M. Rudner, and M. Kolodrubetz, Quasiperiodic Floquet-Thouless energy pump, *Phys. Rev. Lett.* **127**, 166804 (2021).
- [27] M. H. Kolodrubetz, F. Nathan, S. Gazit, T. Morimoto, and J. E. Moore, Topological Floquet-Thouless energy pump, *Phys. Rev. Lett.* **120**, 150601 (2018).
- [28] L. K. Upreti, C. Evain, S. Randoux, P. Suret, A. Amo, and P. Delplace, Topological swing of Bloch oscillations in quantum walks, *Phys. Rev. Lett.* **125**, 186804 (2020).
- [29] A. F. Adiyatullin, L. K. Upreti, C. Lechevalier, C. Evain, F. Copie, P. Suret, S. Randoux, P. Delplace, and A. Amo, Topological properties of Floquet winding bands in a photonic lattice, *Phys. Rev. Lett.* **130**, 056901 (2023).
- [30] Z. Zhu, M. Gächter, A.-S. Walter, K. Viebahn, and T. Esslinger, Reversal of quantised Hall drifts at non-interacting and interacting topological boundaries, [arXiv:2301.03583](https://arxiv.org/abs/2301.03583).
- [31] J. Ningyuan, C. Owens, A. Sommer, D. Schuster, and J. Simon, Time- and site-resolved dynamics in a topological circuit, *Phys. Rev. X* **5**, 021031 (2015).
- [32] V. V. Albert, L. I. Glazman, and L. Jiang, Topological properties of linear circuit lattices, *Phys. Rev. Lett.* **114**, 173902 (2015).
- [33] C. H. Lee, S. Imhof, C. Berger, F. Bayer, J. Brehm, L. W. Molenkamp, T. Kiessling, and R. Thomale, Topoelectrical circuits, *Commun. Phys.* **1**, 39 (2018).
- [34] T. Helbig, T. Hofmann, C. H. Lee, R. Thomale, S. Imhof, L. W. Molenkamp, and T. Kiessling, Band structure engineering and reconstruction in electric circuit networks, *Phys. Rev. B* **99**, 161114(R) (2019).
- [35] T. Hofmann, T. Helbig, F. Schindler, N. Salgo, M. Brzezińska, M. Greiter, T. Kiessling, D. Wolf, A. Vollhardt, A. Kabaš, C. H. Lee, A. Bilušić, R. Thomale, and T. Neupert, Reciprocal skin effect and its realization in a topoelectrical circuit, *Phys. Rev. Res.* **2**, 023265 (2020).
- [36] A. Stegmaier, S. Imhof, T. Helbig, T. Hofmann, C. H. Lee, M. Kremer, A. Fritzsche, T. Feichtner, S. Klembt, S. Höfling, I. Boettcher, I. C. Fulga, L. Ma, O. G. Schmidt, M. Greiter, T. Kiessling, A. Szameit, and R. Thomale, Topological defect engineering and \mathcal{PT} symmetry in non-Hermitian electrical circuits, *Phys. Rev. Lett.* **126**, 215302 (2021).

- [37] H. Hohmann, T. Hofmann, T. Helbig, S. Imhof, H. Brand, L. K. Upreti, A. Stegmaier, A. Fritzsche, T. Müller, U. Schwingenschlögl, C. H. Lee, M. Greiter, L. W. Molenkamp, T. Kießling, and R. Thomale, Observation of cnoidal wave localization in nonlinear topoelectrical circuits, *Phys. Rev. Res.* **5**, L012041 (2023).
- [38] X. Zhang, B. Zhang, H. Sahin, Z. B. Siu, S. M. Rafi-Ul-Islam, J. F. Kong, M. B. A. Jalil, R. Thomale, and C. H. Lee, Anomalous fractal scaling in two-dimensional electric networks, *Commun. Phys.* **6**, 151 (2023).
- [39] K. Yatsugi, T. Yoshida, T. Mizoguchi, Y. Kuno, H. Iizuka, Y. Tadokoro, and Y. Hatsugai, Observation of bulk-edge correspondence in topological pumping based on a tunable electric circuit, *Commun. Phys.* **5**, 180 (2022).
- [40] Y. Wang, H. M. Price, B. Zhang, and Y. D. Chong, Circuit implementation of a four-dimensional topological insulator, *Nat. Commun.* **11**, 2356 (2020).
- [41] T. Hofmann, T. Helbig, C. H. Lee, M. Greiter, and R. Thomale, Chiral voltage propagation and calibration in a topoelectrical Chern circuit, *Phys. Rev. Lett.* **122**, 247702 (2019).
- [42] T. Helbig, T. Hofmann, S. Imhof, M. Abdelghany, T. Kiessling, L. W. Molenkamp, C. H. Lee, A. Szameit, M. Greiter, and R. Thomale, Generalized bulk–boundary correspondence in non-Hermitian topoelectrical circuits, *Nat. Phys.* **16**, 747 (2020).
- [43] D. Zou, T. Chen, W. He, J. Bao, C. H. Lee, H. Sun, and X. Zhang, Observation of hybrid higher-order skin-topological effect in non-Hermitian topoelectrical circuits, *Nat. Commun.* **12**, 7201 (2021).
- [44] T. Kotwal, F. Moseley, A. Stegmaier, S. Imhof, H. Brand, T. Kießling, R. Thomale, H. Ronellenfitsch, and J. Dunkel, Active topoelectrical circuits, *Proc. Natl. Acad. Sci. USA* **118**, e2106411118 (2021).
- [45] M. Ezawa, Electric circuits for non-Hermitian Chern insulators, *Phys. Rev. B* **100**, 081401(R) (2019).
- [46] S. M. Rafi-Ul-Islam, Z. B. Siu, and M. B. A. Jalil, Non-Hermitian topological phases and exceptional lines in topoelectrical circuits, *New J. Phys.* **23**, 033014 (2021).
- [47] N. A. Olekhno, E. I. Kretov, A. A. Stepanenko, P. A. Ivanova, V. V. Yaroshenko, E. M. Puhtina, D. S. Filonov, B. Cappello, L. Matekovits, and M. A. Gorlach, Topological edge states of interacting photon pairs emulated in a topoelectrical circuit, *Nat. Commun.* **11**, 1436 (2020).
- [48] X. Ni, Z. Xiao, A. B. Khanikaev, and A. Alù, Robust multiplexing with topoelectrical higher-order Chern insulators, *Phys. Rev. Appl.* **13**, 064031 (2020).
- [49] J. Yao, X. Hao, B. Song, Y. Jia, C. Hua, and M. Zhou, Majorana-like end states in one-dimensional dimerized Kitaev topoelectrical circuit, *New J. Phys.* **24**, 043032 (2022).
- [50] R.-L. Zhang, Q.-P. Wu, M.-R. Liu, X.-B. Xiao, and Z.-F. Liu, Complex-real transformation of eigenenergies and topological edge states in square-root non-Hermitian topoelectrical circuits, *Ann. Phys. (Leipzig)* **534**, 2100497 (2022).
- [51] A. Darabi, X. Ni, M. Leamy, and A. Alù, Reconfigurable Floquet elastodynamic topological insulator based on synthetic angular momentum bias, *Sci. Adv.* **6**, eaba8656 (2020).
- [52] A. Nagulu, X. Ni, A. Kord, M. Tymchenko, S. Garikapati, A. Alù, and H. Krishnaswamy, Chip-scale floquet topological insulators for 5G wireless systems, *Nat. Electron.* **5**, 300 (2022).
- [53] P. G. Harper, Single band motion of conduction electrons in a uniform magnetic field, *Proc. Phys. Soc. London, Sect. A* **68**, 874 (1955).
- [54] S. Aubry and G. André, Analyticity breaking and Anderson localization in incommensurate lattices, *Ann. Isr. Phys. Soc.* **3**, 18 (1980).
- [55] Y. E. Kraus, Y. Lahini, Z. Ringel, M. Verbin, and O. Zilberberg, Topological states and adiabatic pumping in quasicrystals, *Phys. Rev. Lett.* **109**, 106402 (2012).
- [56] Y. E. Kraus, Z. Ringel, and O. Zilberberg, Four-dimensional quantum Hall effect in a two-dimensional quasicrystal, *Phys. Rev. Lett.* **111**, 226401 (2013).
- [57] Y. Hatsugai, Chern number and edge states in the integer quantum Hall effect, *Phys. Rev. Lett.* **71**, 3697 (1993).
- [58] H. Nassar, H. Chen, A. N. Norris, and G. L. Huang, Quantization of band tilting in modulated phononic crystals, *Phys. Rev. B* **97**, 014305 (2018).
- [59] L. Li, S. Mu, C. H. Lee, and J. Gong, Quantized classical response from spectral winding topology, *Nat. Commun.* **12**, 5294 (2021).